Characterization of the spatiotemporal evolution of laser-generated plasmas

E. P. Kanter,[1,a)] R. Santra,[1,2] C. Höhr,[1,b)] E. R. Peterson,[1,c)] J. Rudati,[1,d)] D. A. Arms,[1] E. M. Dufresne,[1] R. W. Dunford,[1] D. L. Ederer,[1,e)] B. Krässig,[1] E. C. Landahl,[1,f)] S. H. Southworth,[1] and L. Young[1]
[1]*Argonne National Laboratory, Argonne, Illinois 60439, USA*
[2]*Department of Physics, University of Chicago, Chicago, Illinois 60637, USA*

(Received 1 July 2008; accepted 12 August 2008; published online 9 October 2008)

We characterize the time evolution of ion spatial distributions in a laser-produced plasma. Krypton ions are produced in strong, linearly and circularly polarized optical laser fields ($10^{14}-10^{15}$ W/cm^2). The Kr^+ ions are preferentially detected by resonant x-ray absorption. Using microfocused, tunable x rays from Argonne's Advanced Photon Source, we measure ion densities as a function of time with 10 μm spatial resolution for times $\leq$50 ns. For plasma densities of the order of 10^{14} cm^{-3}, we observe a systematic expansion of the ions outward from the laser focus. We find the expansion timescale to be independent of the plasma density though strongly dependent on the plasma shape and electron temperature. The former is defined by the laser focus, while the latter is controlled by the laser polarization state. We have developed a fluid description assuming a collisionless quasineutral plasma, which is modeled using a particle-in-cell approach. This simulation provides a quantitative description of the observed behavior and demonstrates the role of the very different electron temperatures produced by circularly and linearly polarized light. These results demonstrate the utility of this method as an *in situ* probe of the time and spatial evolution of laser-produced plasmas. © *2008 American Institute of Physics*. [DOI: 10.1063/1.2991339]

I. INTRODUCTION

With the rapid advance in laser technology over recent decades, femtosecond-duration optical pulses are now commonplace. When focused to submillimeter dimensions on gaseous or solid samples, the strong electric fields present in such laser pulses produce transient plasmas by ionization of outer shell electrons in matter exposed to them. These laser-produced plasmas (LPPs) are now ubiquitous in laboratories around the world. LPPs have been objects of intense study due to their central role in the development of x-ray lasers,[1,2] inertial confinement fusion,[3] and advanced accelerator concepts.[4] These plasmas are transient and usually not in thermodynamic equilibrium. Consequently, complex models are required to predict behavior, often with limited success.[5] It was suggested that tailored plasmas, suitable for recombination x-ray lasing schemes, could be achieved by tunnel ionization of gases.[6] Subsequently, plasmas produced by strong-field ionization of gaseous targets in the long-wavelength, long-pulse (10 μm, 500 ps) (Refs. 7 and 8) and short wavelength, short-pulse (1–0.5 μm, subpicosecond)[9,10] regimes were studied. Those experiments probed medium density plasmas (10^{18}/cm^3) using x-ray emission and optical Thomson scattering to characterize electron temperatures and showed qualitative, but limited quantitative, agreement with models. Novel double pulse techniques[11] have also used soft x-ray emission from laser-ablated metals to probe the spatiotemporal dynamics of such plasmas.[12] Such measurements are complicated by the self absorption of the soft x rays and have shown similarly limited quantitative agreement with theory.[13] Furthermore, no information is obtained on ground state ion or neutral populations using emission methods. For such information absorption methods are required. In denser plasmas (10^{23}/cm^3) direct absorption using an "x-ray backlighter" continuum, generated by laser irradiation of a high-Z target, is feasible.[5,14] However, direct absorption methods have been limited to dense targets where the plasma complexity prevents the extraction of individual state-to-state cross sections used in modeling.

Recently, it was demonstrated that ion imaging techniques can provide an *in situ* probe of ion density profiles in an LPP.[15] Here we introduce the power of synchrotron-based x-ray microprobe methodology[16] to investigate the evolution of those density profiles with time and spatial resolutions at the 100 ps and 10 μm level, respectively. The brilliance of the synchrotron allows us to probe lower density plasmas ($\sim 10^{14}$/cm^3), which presents a challenge to other methods. The tunability of the synchrotron light permits the use of resonant x-ray absorption, which allows us to distinguish ions from neutrals with high contrast. Because of the penetrating power of the hard x-ray probe, this method is readily scalable to much denser plasmas as well.

II. EXPERIMENT

The experiments were performed at beamline 7-ID of Argonne's Advanced Photon Source (APS) in combination

[a)]Electronic mail: kanter@anl.gov.
[b)]Present address: TRIUMF, Vancouver, BC V6T2A3, Canada.
[c)]Present address: Osram Sylvania, Inc., Beverly, MA, USA.
[d)]Present address: Xradia Inc., Concord, CA 94520, USA.
[e)]Present address: Louisiana State University, Baton Rouge, LA 70809,USA.
[f)]Present address: Department of Physics, DePaul University, Chicago, IL 60614, USA.

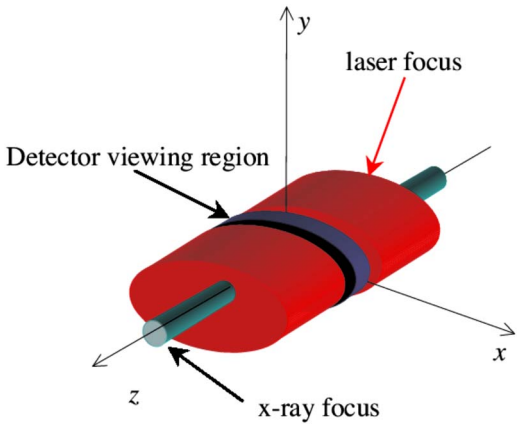

FIG. 1. (Color online) Schematic representation of laser and x-ray foci in the transverse (xy) plane. The volume shown represents the Rayleigh range of the laser focus while the dark banded region demonstrates the narrow slice of the plasma viewed by the detectors. The x-ray probe samples the plasma at various locations along the vertical y-axis to obtain spatial distributions in the transverse plane. In practice, this is achieved by translating the laser focus vertically. It can also be translated along the z-axis to obtain longitudinal distributions.

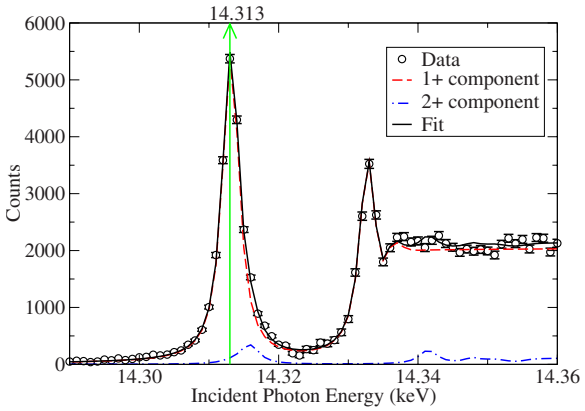

FIG. 2. (Color online) Measured x-ray absorption spectrum showing fitted Kr^+ and Kr^{2+} contributions. A small neutral contribution has already been subtracted. The fit procedure is described in Ref. 17. The arrow indicates the Kr^+ $1s \rightarrow 4p$ excitation energy of 14.313 keV where ion density measurements were carried out.

with a Ti:sapphire ultrafast laser system that is phase-locked to the radio frequency clock of the storage ring. Typical laser parameters were 800 nm wavelength, 1 mJ/pulse, and pulse length of 65 fs, focused to 92×46 μm^2 full width at half maximum (FWHM) with a ~1 kHz repetition frequency. Detailed descriptions of the laser system and its synchronization with the x-ray pulses have previously been given.[17–19] A variety of measurements was made with different gas targets, laser intensities, and polarizations. Common to all measurements was a copropagating geometry between the laser and x-ray beams (crossing angle $\lesssim 1°$) with a common focus in the gas target (see Fig. 1). The laser focus was intentionally broader in the transverse direction than the x-ray beam to exploit the x rays as a probe of the spatial extent of the plasma. Targets were gaseous Kr atoms produced either in an effusive gas jet[16] for the lower densities studied ($\sim 10^{13}$–$10^{14}/cm^3$) or in a small gas cell[17] at higher densities ($\sim 10^{15}/cm^3$).

In our microprobe,[16] we used x rays from an undulator at Sector 7 of the APS, which were monochromatized (bandwidth of ~0.8 eV) and tuned to 14.313 keV. This photon energy corresponds to the excitation of the Kr^+ $1s \rightarrow 4p$ resonance that is absent in the nonionized Kr ($4p^6$) background and thus provides a definitive signature of the laser-ionized plasma. In earlier experiments with somewhat higher laser intensities, where multiply ionized Kr ions were more abundant, the contribution of Kr^{2+} was found to be ~18% at that photon energy.[17] Here, we adjusted laser parameters such that the contribution of Kr^{2+} was <2% (see Fig. 2) in order to obtain a simple two component plasma whose properties we could control.

The x rays were focused efficiently by a large-aperture, dynamically bent Kirkpatrick–Baez mirror pair[20] to a FWHM diameter of <10 μm. The x-ray flux after focusing is $\sim 10^6$ photons/pulse in ~100 ps pulses with a repetition rate of 272 kHz and energy resolution $\Delta E/E \sim 10^{-4}$. Hard x rays, emitted from the interaction region, were recorded by a pair of energy-dispersive Si-drift detectors placed at 90° to, and in the plane of polarization of, the x-ray beam. In this geometry, Rayleigh and Compton x-ray scattering are minimized, and we observe primarily $K\alpha\beta$ fluorescence from the prompt decay of the Kr^+ resonance. The yield of the $K\alpha$ fluorescence is proportional to the ion density in the cylindrical volume probed by the x rays and viewed by the detectors.

Spatial overlap of the laser and x-ray beams is accomplished initially by scanning sharp vertical and horizontal edges through each beam and adjusting the laser optics accordingly. Temporal overlap is achieved in two steps. A crude overlap is established by observing individually the laser and x-ray signals on an InGaAs photodiode downstream of the interaction region and noting the time, relative to a fiducial photodiode signal produced by the laser upstream of the final optics. Because ions can still be present for several hundred nanoseconds after the laser pulse, this procedure is adequate in adjusting to adjust the timing between the fs laser pulses and the ~100 ps x-ray pulses so that $K\alpha$ fluorescence can be observed from the ions in the x-ray beam. That signal can then be used to fine tune the overlap of the beams both spatially and temporally by maximizing the fluorescence.

The Kr $K\alpha$ emission was recorded in two scalers that were separately gated from each orbital period of the synchrotron, corresponding to whether or not the x-ray pulses were within ± 1 μs of the laser pulse. Because of the higher frequency of the x-ray beam compared to the laser, we measured 271 "laser off" x-ray pulses for each "laser on" pulse. We recorded those scalar values for various vertical displacements (the y coordinate) of the laser beam relative to the x rays and for different delays of the x rays (t) relative to the optimized overlap time ($t=0$) thus obtaining time-resolved spatial distributions. In this manner, the detectors' view of the x-ray focus region remains fixed (see Fig. 1), while the plasma is displaced in position and in time relative to the x-ray focus. Further experimental details can be found in Ref. 17. Note that for the case of those measurements with

linear polarization, the laser polarization was parallel to the x-ray polarization in the horizontal (x) plane.

III. ANALYSIS AND RESULTS

To observe the ion dynamics within the LPP, we investigated both the temporal and spatial dependence of the ion densities as reflected in the ratios of the Kr $K\alpha$ emission following the laser on and laser off x-ray pulses. Although all atoms at the center of the laser focus may be ionized, the ion density falls off transverse to the beams (x,y coordinates) in regions of weaker laser field, leaving a background of neutral Kr atoms. As the ion cloud expands through these regions, we must correct for that stationary neutral background.

We consider a two-component system of neutrals and Kr^+ ions. As indicated in Fig. 1, the width of the detector viewing region is small (~ 1 mm) compared to the longitudinal extent of the plasma ($2z_0 \sim 1.2$ cm, with z_0 representing the Rayleigh range of the laser focus). Thus, we observe the ion motion in a transverse plane defined by the detector collimation and neglect any longitudinal dependence of the densities. We define the ion density in the transverse plane as $n_i(x,y,t)$, the neutral density in that plane as $n_0(x,y,t)$, and the uniform gas density in the target region as n. If α is the ratio of the photoexcitation cross section of the ions to that of the neutrals (at the measurement energy of 14.313 keV), then the space- and time-dependent ratio

$$R(x,y,t) = \frac{\alpha n_i + n_0}{n}, \tag{1a}$$

$$= \alpha \frac{n_i}{n} + \frac{n_0}{n}, \tag{1b}$$

is the experimentally measured ratio of laser on/laser off $K\alpha$ fluorescence. At $t=0$,

$$n_i(x,y,0) + n_0(x,y,0) = n, \tag{2}$$

and the thermal neutral motion is slow compared to the ion motion so that $n_0(x,y,t) = n_0(x,y,0)$ for small t compared to the observed $\sim \mu$s neutralization time. We further assume that at $t=0$, ionization is near saturation at the origin so that $R_0 = R(0,0,0) \simeq \alpha$. Saturation implies the absence of neutrals in such a region, and from Eqs. (1) and (2) the value R_0 then simply reflects the ratio α of K shell excitation cross sections for Kr^+/Kr. With these assumptions, it is then straightforward to show that the normalized ion density d_n can be expressed as

$$d_n(x,y,t) = \frac{n_i(x,y,t)}{n} \tag{3a}$$

$$= \frac{R(x,y,t) - 1}{R_0} + \frac{R(x,y,0) - 1}{R_0(R_0 - 1)}. \tag{3b}$$

Because $R_0 \gg 1$ (~ 50), and the background term decreases quadratically with R_0, this correction is $\sim 2\%$ and hence comparable to other experimental errors. The correction amounts to $\sim 2\%$ of the initial $t=0$ distribution applied to each $t>0$ distribution. In general, this is a very small but systematic effect. Note also that wherever $R(x,y,0)$ is saturated, this reduces to the limit of

$$\frac{n_i(x,y,t)}{n} = \frac{R(x,y,t)}{R_0}. \tag{4}$$

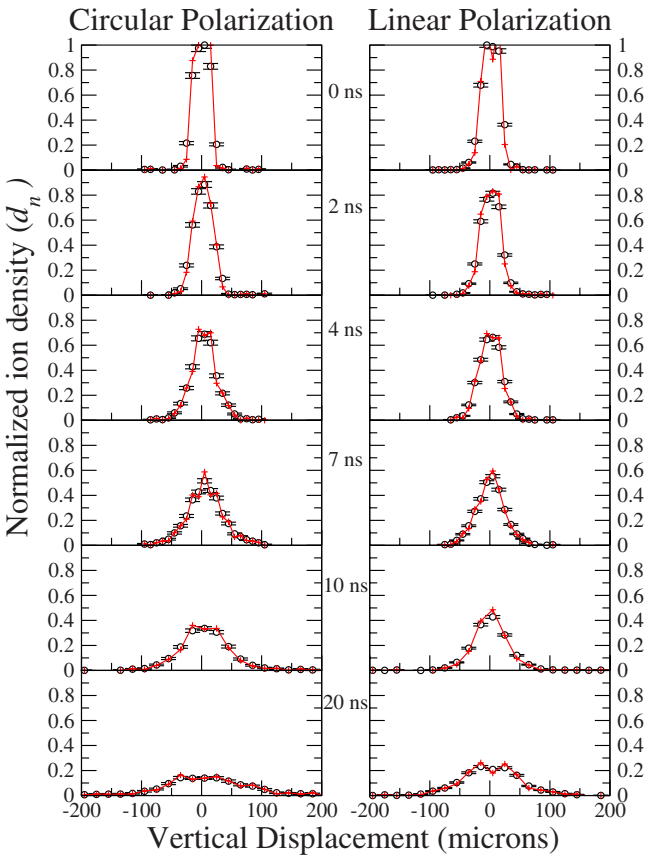

FIG. 3. (Color online) Spatial distributions of Kr^+ ions for various delays between the x-ray probe beam and the laser-induced ionization. Plotted is the dimensionless normalized ion density d_n as defined in Eq. (2). At saturation ($x=y=t=0$) the value is 1. The solid lines show the effect of deconvoluting the 10 μm Gaussian x-ray beam profile. The difference is barely observable at $t=0$ and inconsequential at longer times.

Figure 3 shows a plot of the quantity d_n for various values of the time delay t. These data were obtained by moving the laser beam vertically (y direction) but keeping the x-ray, gas-jet, and detector geometries fixed. Hence, these are measurements of the normalized ion density as a function of transverse distance from the center of the laser focus. Several features of these data are noteworthy. First, there is apparently little change in the shapes of the distributions for the first few nanoseconds. Then, for $t \gtrsim 2$ ns, we observe a systematic widening and simultaneous decrease in amplitude as the ions spread out spatially. Furthermore, it is apparent that the timescale of this expansion in the case of circular polarization is faster than that of linear polarization. We have found those general features common at all gas densities studied.

To quantify these data, we have investigated these distributions further as shown in Fig. 4. In the top panel of Fig. 4(a), we plot the peak value of each spatial distribution, corresponding to $y=0$ in each panel of Fig. 3, as a function of

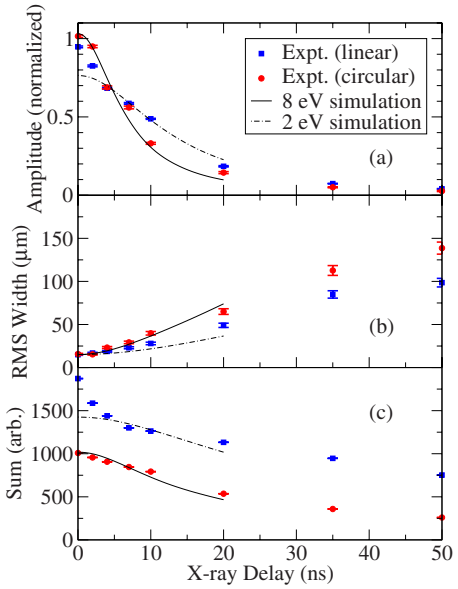

FIG. 4. (Color online) The time evolution of various features of the experimental spatial profiles. Lines show the results of the model simulation for different initial electron temperatures. A 2:1 $(x:y)$ aspect ratio was assumed for the initial plasma geometry (at $t=0$) as shown in Fig. 1. The central amplitude (value at $x=y=0$) is plotted in (a) while (b) shows the rms width of each of the distributions of Fig. 3. The sum of each distribution is plotted in (c). The apparent rapid decrease in the case of the linear polarization data seen for $t<5$ ns in (a) and (c) is a consequence of dealignment (Ref. 21) as described in the text.

x-ray delay time t quantifying the decrease in amplitude noted above. The middle panel of Fig. 4(b) shows the growth of the root mean square (rms) radius σ of each distribution. Finally, the bottom panel of Fig. 4(c) shows the integral of each distribution as a function of t. As our data represent one-dimensional scans while the plasma is expanding in three dimensions, Fig. 4 shows a decrease with t in this integral, suggesting loss of ions from the one-dimensional slice being considered. In order to understand these properties, we have simulated the behavior of such LPPs.

IV. SIMULATIONS

A defining property of a plasma is that it be quasineutral,[22] i.e., the electron density $n_e(\boldsymbol{x},t)$ be approximately equal to the ion density $n_i(\boldsymbol{x},t)$, assuming for simplicity that there is only one ion species. For quasineutrality to hold, the electron Debye length λ_D must be much smaller than the spatial extension of the electron-ion mixture. Assuming an electron density of $n_e=10^{14}$ cm^{-3} and an electron temperature of $T_e=1$ eV, $\lambda_D=0.7$ μm. This is indeed much smaller than the typical transverse dimension of the ionized gas volumes studied in our experiments (~ 45 μm). So, we may call our electron-ion mixtures plasmas in the most traditional sense, and we should expect them to maintain quasineutrality.

The relative importance of collective plasma motion in comparison to individual particle-particle collisions in a plasma is characterized by N_D, the number of electrons in a sphere of radius equal to the electron Debye length.[22,23] The criterion that the electron-ion mixture be dominated by collective effects rather than collisions, i.e., $N_D \gg 1$, is a second defining property of a plasma. If the electron density n_e is given in cm^{-3} and the electron temperature T_e is given in eV, then

$$N_D = 1.7 \times 10^9 \sqrt{T_e^3/n_e}. \tag{5}$$

For our typical densities and temperatures, $n_e \simeq 10^{14}$ cm^{-3} and $T_e \simeq 1$ eV; hence $N_D \simeq 170$. Therefore, it seems justified to assume that for our purposes, the plasmas we produce are collisionless (ideal plasmas).

Collisionless plasma behavior is described completely by the Vlasov equation[22,23] combined with Maxwell's equations. By taking moments, with respect to velocity, of the Vlasov equation, fluid equations for the plasma are obtained as[22,23]

$$\frac{\partial n_j}{\partial t} + \nabla \cdot (n_j \boldsymbol{v}_j) = 0, \tag{6}$$

$$m_j n_j \left[\frac{\partial \boldsymbol{v}_j}{\partial t} + (\boldsymbol{v}_j \cdot \nabla)\boldsymbol{v}_j \right] = n_j q_j \left(\boldsymbol{E} + \frac{\boldsymbol{v}_j}{c} \times \boldsymbol{B} \right) - \nabla p_j. \tag{7}$$

In these equations, j indicates the species ($j=e$ for electrons, $j=i$ for ions), $n_j(\boldsymbol{x},t)$ is the particle density, $\boldsymbol{v}_j(\boldsymbol{x},t)$ is the velocity of the fluid, q_j is the charge of a particle of species j, m_j is the mass of a particle of species j, $\boldsymbol{E}(\boldsymbol{x},t)$ is the electric field, $\boldsymbol{B}(\boldsymbol{x},t)$ is the magnetic field, c is the speed of light, and $p_j(\boldsymbol{x},t)$ is the pressure of species j. The pressure term is written assuming that the velocity distribution function of the particles comprising the electron and ion fluids is an isotropic Maxwellian.

In order to describe the expansion of a collisionless plasma into a vacuum, the following assumptions are made (see Ref. 24 and references therein). First, as long as $|\boldsymbol{v}_j(\boldsymbol{x},t)| \ll c$ and assuming that no strong external magnetic field is imposed, the Lorentz force may be neglected. The ions are treated as a cold fluid so that the ion pressure $p_i = 0$. Hence, as far as the ions are concerned,

$$\frac{\partial n_i}{\partial t} + \nabla \cdot (n_i \boldsymbol{v}_i) = 0, \tag{8}$$

$$\frac{\partial \boldsymbol{v}_i}{\partial t} + (\boldsymbol{v}_i \cdot \nabla)\boldsymbol{v}_i = \frac{q_i}{m_i}\boldsymbol{E}. \tag{9}$$

The electron fluid is assumed to remain in thermal equilibrium throughout each integration step (as will be described below), with a position-independent temperature T_e, so that the electron pressure may be written as

$$p_e = n_e T_e \tag{10}$$

(Since we measure temperature in units of energy, the Boltzmann constant equals unity.) Therefore, assuming that the electrons respond adiabatically to $\boldsymbol{E}$ (and thus to the ion fluid), i.e.,

$$\frac{d\boldsymbol{v}_e}{dt} = \frac{\partial \boldsymbol{v}_e}{\partial t} + (\boldsymbol{v}_e \cdot \nabla)\boldsymbol{v}_e = \boldsymbol{0}, \tag{11}$$

it follows from Eqs. (7) and (10) that

$$\boldsymbol{E} = \frac{T_e}{q_e}\frac{\boldsymbol{\nabla} n_e}{n_e}. \tag{12}$$

Mora[24] combined this equation with Poisson's equation and solved the resulting set of equations self-consistently during each time step for the ion fluid.

Here, we pursue a simpler (and less accurate) approach and enforce the requirement that the plasma be quasineutral. Let $Z_i = -q_i/q_e$ denote the ion charge. Then, within the plasma approximation,[22] we enforce quasineutrality by setting $n_e = Z_i n_i$. Using this, the electric field $\boldsymbol{E}$ given in Eq. (12) is inserted in Eq. (9):

$$\frac{d\boldsymbol{v}_i}{dt} = \frac{\partial \boldsymbol{v}_i}{\partial t} + (\boldsymbol{v}_i \cdot \boldsymbol{\nabla})\boldsymbol{v}_i = -\frac{Z_i T_e}{m_i}\frac{\boldsymbol{\nabla} n_i}{n_i}. \tag{13}$$

An analogous expression may be found in Ref. 23. The ratio $Z_i T_e/m_i$ is the square of the ion sound velocity. Equation (13) has to be solved together with the continuity equation (8). An important insight provided immediately by Eqs. (8) and (13) is that if $n_i, \mathbf{v}_i$ are solutions, so are βn_i and $\boldsymbol{v}_i$, where $\beta > 0$. This means that the absolute plasma density has no impact on the expansion dynamics. This behavior has been confirmed in our experiments and reported previously.[21] It is only the shape of the plasma that plays a role within this model. Also note that the force acting on a fluid element is proportional to the ion charge and the electron temperature.

In order to estimate the initial electron temperature for our laser parameters, we combine a theory of strong-field ionization of Kr (Ref. 25) with a classical model for the motion of the ionized electron in the laser field.[26] In essence, for a given pulse duration, we numerically integrate rate equations to determine, as a function of the peak intensity I of the pulse, the ionization probability $p(I)$ and the associated electron energy distribution $\tilde{f}(\varepsilon; I)$, where ε is the electron energy and $\int_0^\infty d\varepsilon \tilde{f}(\varepsilon; I) = p(I)$. We then use this information, given a spatial intensity profile $I(\boldsymbol{x})$, to calculate the spatial integral over $\tilde{f}(\varepsilon; I(\boldsymbol{x}))$. After normalization, we obtain from this the kinetic energy distribution of the plasma electrons $f(\varepsilon)$ right after the laser pulse. The electron temperature is then obtained as

$$T_e = \frac{2}{3}\int_0^\infty \varepsilon f(\varepsilon) d\varepsilon. \tag{14}$$

The initial electron temperatures estimated this way for a laser intensity of 1.6×10^{14} W/cm^2 are ~1 eV for linear polarization and ~5 eV for circular polarization.

To solve Eqs. (8) and (13) numerically, we adopt a particle-in-cell strategy.[27] The continuity equation may be trivially satisfied by conserving the number of ions (our particles) in the simulation. The acceleration $d\boldsymbol{v}_i/dt$ of a given ion is obtained from Eq. (13). The temporal integration of the position and velocity equations of motion is performed using the Euler algorithm. At each time step, the ion density, defined at the center of each cell, is employed to calculate $\boldsymbol{\nabla} n_i$ using second-order finite differencing. This allows us to determine at the cell centers the right-hand side of Eq. (13). The acceleration of a given ion, which is generally not located at a cell center, is then obtained by interpolation from the cell centers surrounding the ion. After the ion positions are advanced by one time step, interpolation from the new ion positions is utilized to construct an update for the ion density at the cell centers. Exploiting energy conservation and neglecting the electrostatic contribution to the total energy, the kinetic energy of the ions determined in a given time step is used to update the electron temperature. As a consequence, within this model the electron gas cools adiabatically during the plasma expansion.

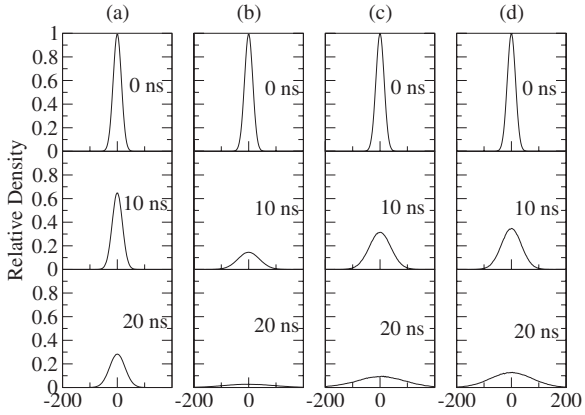

FIG. 5. Simulated spatial distributions of Kr^+ ions for various delays between the x-ray probe beam and the laser-induced ionization. The four different columns correspond to different simulation conditions with (a)–(c) showing results for isothermal expansion, while (d) incorporates adiabatic cooling of the electrons as described above. The initial conditions are as follows: (a) 1 eV electron temperature and 1:1 $x:y$ aspect ratio of the laser focus, (b) 8 eV electron temperature and 1:1 aspect ratio, (c) 8 eV temperature and 3:1 aspect ratio, and (d) 8 eV initial temperature with adiabatic cooling and 3:1 aspect ratio. Plotted is the normalized ion density relative to the value at $x=y=t=0$. The starting $t=0$ y-distributions are identical in all four cases.

Figure 5 shows the spatial distribution of ions for three different times resulting from these simulations for various sets of initial conditions. Parameters varied include the initial electron temperature, the $x:y$ aspect ratio of the plasma geometry, and whether or not the electron temperature was allowed to cool during expansion. These results demonstrate the parameter space available to describe these data as well as the sensitivity of the results to these variations.

V. DISCUSSION

A comparison of the results of the simulations with the experimental data is given in Fig. 4 where the simulated results are shown as curves in each panel. Although the data extend out as far as 50 ns, for practical reasons, the simulations could only be carried out to 20 ns. Nevertheless, the general trends are in good agreement. One feature that is clearly shown in all three panels is a saturation behavior as the curves flatten out at long times. It was this observation that necessitated the inclusion of electron cooling in the simulations. In isothermal simulations, the results would either be a monotonic increase (in the case of the rms widths in the middle panel) or decrease to zero (in the upper and lower panels). By using the adiabatic model described above, the electron cooling leads to saturation at finite delay times, consistent with the data.

The bottom panel, which shows the integrated yield in a slice (Σ), demonstrates the sensitivity of this parameter to the ellipticity of the laser beam focus. In the experiments, the laser optics produced a focus with an $x:y$ aspect ratio of $\sim 2:1$, and hence the resulting plasma was also expected to be elliptical in the transverse plane. Comparing simulations with 1:1, 2:1, and 3:1 ratios (see Fig. 5), we found the 2:1 ratio to indeed fit the data best. The quantity Σ is most sensitive to this feature of the electrorheology of the plasma.[28] Because of the difference in Coulomb force components acting along the shorter dimension of the plasma compared to the longer extent, there is a departure from spherical symmetry. While the total three-dimensional integral would necessarily conserve particles, this one-dimensional integral does not as the Coulomb forces tend to symmetrize the density. This effect is demonstrated in Fig. 5 where the rate of decrease in area of the vertical distributions as a function of time is slowed as the initial horizontal spread is increased (compare columns *b* and *c*). This is a consequence of the reduced horizontal force components, thus tending to symmetrize the distributions. It should also be noted that while the plasma expansion in the case of circular polarization is well-fitted by the simulation, the linear polarization case shows a marked departure at short delay times due to alignment dynamics. These data were taken with the laser polarization parallel to the x-ray polarization. As we showed previously,[21] the alignment produced in the initial ion population under such circumstances leads to an enhanced fluorescence signal at short times; the alignment decays within a few nanoseconds leading to this rapid falloff. This alignment effect is not included in the current simulations.

Beyond the initial shape of the plasma, the only other variable in the simulations was the initial electron *temperature*. In an LPP, the electron energy distributions immediately following ionization are far from equilibrium, and it is difficult to define a temperature *per se*. These initial distributions are determined by the strength of the ionizing field, the electron ionization potential, and the laser polarization[26] as described in Sec. IV. The timescale for thermalizing these initial kinetic energy distributions is inversely proportional to density and for our case of 10^{14} cm^{-3} and a 1 eV distribution is only ~ 400 ps.[29] Therefore, we assumed an initial thermal electron energy distribution in the simulations and allowed that distribution to adiabatically cool as described above. As shown in the middle panel of Fig. 4, the rms width (σ) of each distribution was found to be quite sensitive to the initial electron temperature assumed in the simulations. Most importantly, it demonstrates the differing electron energy distributions produced by circularly and linearly polarized light[30] as expected from quasiclassical theory[26] and as we estimated above. Given the limitations of this tunneling model, the thermalization approximation, and experimental uncertainties affecting the laser intensity, the agreement in electron temperatures is much better than should be expected.

The top panel of Fig. 4 shows the time evolution of the height of each distribution (i.e., the value at $y=0$). With the initial electron temperature and ellipticity determined from the other panels, these data are very well described by the simulation. Again, for $t<5$ ns the case of linear polarization shows an enhancement above our model prediction attributable to the decay of the alignment of the initial ion population.[21]

VI. SUMMARY

In summary, we have introduced synchrotron-based x-ray microprobe methodology to provide time-resolved three-dimensional ion density distributions in LPPs. We have here demonstrated imaging in the plane transverse to the x-ray probe, but it is straightforward to extend this technique to full three-dimensional imaging as well. In contrast to the alternate techniques such as absorption imaging[14] or ion imaging,[15] this method produces time-resolved spatial information and is applicable to a broad range of densities, spanning more than eight orders of magnitude, from dilute gases to solid densities. Furthermore, as we have previously reported, it also provides detailed simultaneous spectral[17] and atomic alignment information in the plasma.[16,21] We have also developed a simple fluid-based simulation and with it demonstrated the sensitivity of these time-dependent data to various properties of the plasma expansion, including the initial shape of the plasma and temperature of the electrons. Because of the penetrating power of the hard x rays used in this technique, it could also be of utility in imaging the nanosecond scale time evolution of even denser plasmas such as those found in inertial fusion experiments (~ 500 g/cm^3).[31]

ACKNOWLEDGMENTS

This work was supported by the Chemical Sciences, Geosciences, and Biosciences Division, (and also in the case of the Advanced Photon Source) the Office of Basic Energy Sciences, Office of Science, U.S. Department of Energy under Contract No. DE-AC02-06CH11357.

[1] M. M. Murnane, H. C. Kapteyn, M. D. Rosen, and R. W. Falcone, Science **251**, 531 (1991).
[2] D. L. Matthews, P. L. Hagelstein, M. D. Rosen, M. J. Eckart, N. M. Ceglio, A. U. Hazi, H. Medecki, B. J. MacGowan, J. E. Trebes, B. L. Whitten, E. M. Campbell, C. W. Hatcher, A. M. Hawryluk, R. L. Kauffman, L. D. Pleasance, G. Rambach, J. H. Scofield, G. Stone, and T. A. Weaver, Phys. Rev. Lett. **54**, 110 (1985).
[3] J. Nuckolls, L. Wood, A. Thiessen, and G. Zimmerman, Nature (London) **239**, 139 (1972).
[4] T. Tajima and J. M. Dawson, Phys. Rev. Lett. **43**, 267 (1979).
[5] M. Fajardo, P. Audebert, P. Renaudin, H. Yashiro, R. Shepherd, J. C. Gauthier, and C. Chenais-Popovics, Phys. Rev. Lett. **86**, 1231 (2001).
[6] N. H. Burnett and P. B. Corkum, J. Opt. Soc. Am. B **6**, 1195 (1989).
[7] W. P. Leemans, C. E. Clayton, W. B. Mori, K. A. Marsh, A. Dyson, and C. Joshi, Phys. Rev. Lett. **68**, 321 (1992).
[8] W. P. Leemans, C. E. Clayton, W. B. Mori, K. A. Marsh, P. K. Kaw, A. Dyson, C. Joshi, and J. M. Wallace, Phys. Rev. A **46**, 1091 (1992).
[9] T. E. Glover, T. D. Donnelly, E. A. Lipman, A. Sullivan, and R. W. Falcone, Phys. Rev. Lett. **73**, 78 (1994).
[10] T. E. Glover, J. K. Crane, M. D. Perry, R. W. Lee, and R. W. Falcone, Phys. Rev. E **57**, 982 (1998).
[11] U. Teubner, G. Kühnle, and F. P. Schäfer, Appl. Phys. Lett. **59**, 2672 (1991).
[12] Y. Okano, K. Oguri, T. Nishikawa, and H. Nakano, Appl. Phys. Lett. **89**, 221502 (2006).
[13] Y. Okano, K. Oguri, T. Nishikawa, and H. Nakano, J. Appl. Phys. **99**, 063302 (2006).
[14] P. Audebert, P. Renaudin, S. Bastiani-Ceccotti, J.-P. Geindre, C. Chenais-Popovics, S. Tzortzakis, V. Nagels-Silvert, R. Shepherd, I. Matsushima, S. Gary, F. Girard, O. Peyrusse, and J.-C. Gauthier, Phys. Rev. Lett. **94**,

025004 (2005).
[15]J. Strohaber and C. Uiterwaal, Phys. Rev. Lett. **100**, 023002 (2008).
[16]L. Young, D. A. Arms, E. M. Dufresne, R. W. Dunford, D. L. Ederer, C. Höhr, E. P. Kanter, B. Krässig, E. C. Landahl, E. R. Peterson, J. Rudati, R. Santra, and S. H. Southworth Phys. Rev. Lett. **97**, 083601 (2006).
[17]S. H. Southworth, D. A. Arms, E. M. Dufresne, R. W. Dunford, D. L. Ederer, C. Höhr, E. P. Kanter, B. Krässig, E. C. Landahl, E. R. Peterson, D. A. Walko, and L. Young, Phys. Rev. A **76**, 043421 (2007).
[18]L. Young, R. W. Dunford, C. Hoehr, E. P. Kanter, B. Krässig, E. R. Peterson, S. H. Southworth, D. L. Ederer, J. Rudati, D. A. Arms, E. M. Dufresne, and E. C. Landahl, Radiat. Phys. Chem. **75**, 1799 (2006).
[19]M. F. DeCamp, D. A. Reis, D. M. Fritz, P. H. Bucksbaum, E. M. Dufresne, and R. Clarke, J. Synchrotron Radiat. **12**, 177 (2005).
[20]P. J. Eng, M. Newville, M. L. Rivers, and S. R. Sutton, in *X-Ray Microfocusing: Applications and Techniques*, Proceedings of SPIE: The International Society for Optical Engineering, edited by I. McNulty (Society of Photo-optical Instrumentation Engineers, Bellingham, WA, 1998), Vol. 3449, pp. 145–155.
[21]C. Höhr, E. R. Peterson, N. Rohringer, J. Rudati, D. A. Arms, E. M. Dufresne, R. W. Dunford, D. L. Ederer, E. P. Kanter, B. Krässig, E. C. Landahl, R. Santra, S. H. Southworth, and L. Young, Phys. Rev. A **75**, 011403(R) (2007).
[22]F. F. Chen, *Introduction to Plasma Physics and Controlled Fusion*, Plasma Physics Vol. 1, 2nd ed. (Springer, New York, 2006).
[23]W. L. Kruer, *The Physics of Laser Plasma Interactions* (Westview, Boulder, CO, 2003).
[24]P. Mora, Phys. Rev. Lett. **90**, 185002 (2003).
[25]R. Santra, R. W. Dunford, and L. Young, Phys. Rev. A **74**, 043403 (2006).
[26]P. B. Corkum, N. H. Burnett, and F. Brunel, Phys. Rev. Lett. **62**, 1259 (1989).
[27]Y. N. Grigoryev, V. A. Vshivkov, and M. P. Fedoruk, *Numerical "Particle-in-Cell" Methods* (VSP BV, Utrecht, 2002).
[28]A. V. Ivlev, G. E. Morfill, H. M. Thomas, C. Räth, G. Joyce, P. Huber, R. Kompaneets, V. E. Fortov, A. M. Lipaev, V. I. Molotkov, T. Reiter, M. Turin, and P. Vinogradov, Phys. Rev. Lett. **100**, 095003 (2008).
[29]P. A. Sturrock, *Plasma Physics* (Cambridge University Press, Cambridge, England, 1994).
[30]P. H. Bucksbaum, M. Bashkansky, R. R. Freeman, T. J. McIlrath, and L. F. DiMauro, Phys. Rev. Lett. **56**, 2590 (1986).
[31]J. R. Rygg, F. H. Seguin, C. K. Li, J. A. Frenje, M. J.-E. Manuel, R. D. Petrasso, R. Betti, J. A. Delettrez, O. V. Gotchev, J. P. Knauer, D. D. Meyerhofer, F. J. Marshall, C. Stoeckl, and W. Theobald, Science **319**, 1223 (2008).